JOURNAL OF COMPUTATIONAL PHYSICS **133,** 205–221 (1997)
ARTICLE NO. CP965468

Thermomechanical Simulation of the Splashing of Ceramic Droplets on a Rigid Substrate

Mauro Bertagnolli,* Maurizio Marchese,* Gianni Jacucci,* Ioannis St. Doltsinis,† and Swen Noelting†

*Dipartimento di Informatica e Studi Aziendali, Laboratorio di Ingegneria Informatica, Universita' di Trento, Trento, Italy; †Institute for Computer Applications, University of Stuttgart, Stuttgart, Germany

Received March 2, 1995; revised January 4, 1996

Finite element simulation techniques have been applied to the spreading process of single ceramic liquid droplets impacting on a flat cold surface under plasma-spraying conditions. The goal of the present investigation is to predict the geometrical form of the splat as a function of technological process parameters, such as initial temperature and velocity, and to follow the thermal field developing in the droplet up to solidification. A non-linear finite element programming system has been utilized in order to model the complex physical phenomena involved in the present impact process. The Lagrangean description of the motion of the viscous melt in the drops, as constrained by surface tension and the developing contact with the target, has been coupled to an analysis of transient thermal phenomena accounting also for the solidification of the material. The present study refers to a parameter spectrum as from experimental data of technological relevance. The significance of process parameters for the most pronounced physical phenomena is discussed as are also the consequences of modelling. We consider the issue of solidification as well and touch on the effect of partially unmelted material.

1. INTRODUCTION

The plasma spray process is a convenient way to coat structural parts with a layer of another material, protecting them from thermal shock or aggressive environment. As in other thermal spray methods, this coating layer is formed by the impingement of small molten particles on the substrate to be coated. In the case of plasma spray, the source of heat that melts the particles of the coating material is a plasma torch, at very high temperature (ca 20,000 K). This manufacturing process has been described in detail elsewhere (see, for example, [1]). The quality of the coating obtained depends on a large number of parameters, like the design and the power of the torch, its position relative to the substrate, the type of powder used, the way it is introduced into the plasma, and the nature and preparation of the substrate. Traditionally, the above process parameters have been optimized empirically.

In recent years, much progress has been made in understanding the physics of plasma spraying, particularly the physics of the plasma and the plasma–particle interactions (see, for instance, [2, 3]). The microstructures of the resulting coatings have been studied by a number of authors [4, 5]. The objective of such studies is to understand how the properties of the coatings correlate with the parameters of the production process. The present account addresses one fundamental issue that influences the final properties of ceramic coatings; namely the heat transfer and material flow phenomena associated with the impingement, spreading, and solidification of liquid droplets on solid cool surfaces.

In the plasma-spray process ceramic or metallic powder is fed into a high temperature, high velocity arc plasma, where the powder particles melt as they are propelled towards the substrate. The molten material then splats onto the substrate to build up the coating. A typical simulation of the single impact event is shown in Fig. 1. The final microstructure of plasma-sprayed coatings is a result of, and depends on, the details of the spraying process. It is influenced i.a. by the velocity, temperature, size distribution, and percentage of molten particles, as well as the conditions of spreading and solidification during impact.

The problem of investigating the in-flight and impact behaviour of the melted particles is presently tackled at different levels:

- information about the heat transfer, fluid flow, and solidification processes is sought by use of laser techniques [6–8], high speed photography [9], or videography [10, 11]. However, such information is difficult to obtain and is available in an extensive form merely for special study cases.
- on the other hand, it is possible to conceive theoretical and numerical models for the investigation of the impact process phenomenom [10–13]. Such models, once validated by experiments, can be used to interpret transient behaviour and to extend experimental knowledge to different parameters' space regions.

The output of such experimental and theoretical studies is also used as the foundation of discrete models for the spraying deposition process [15, 16]. The latter, can ultimately link the single particle behaviour to the final coating

0021-9991/97 $25.00

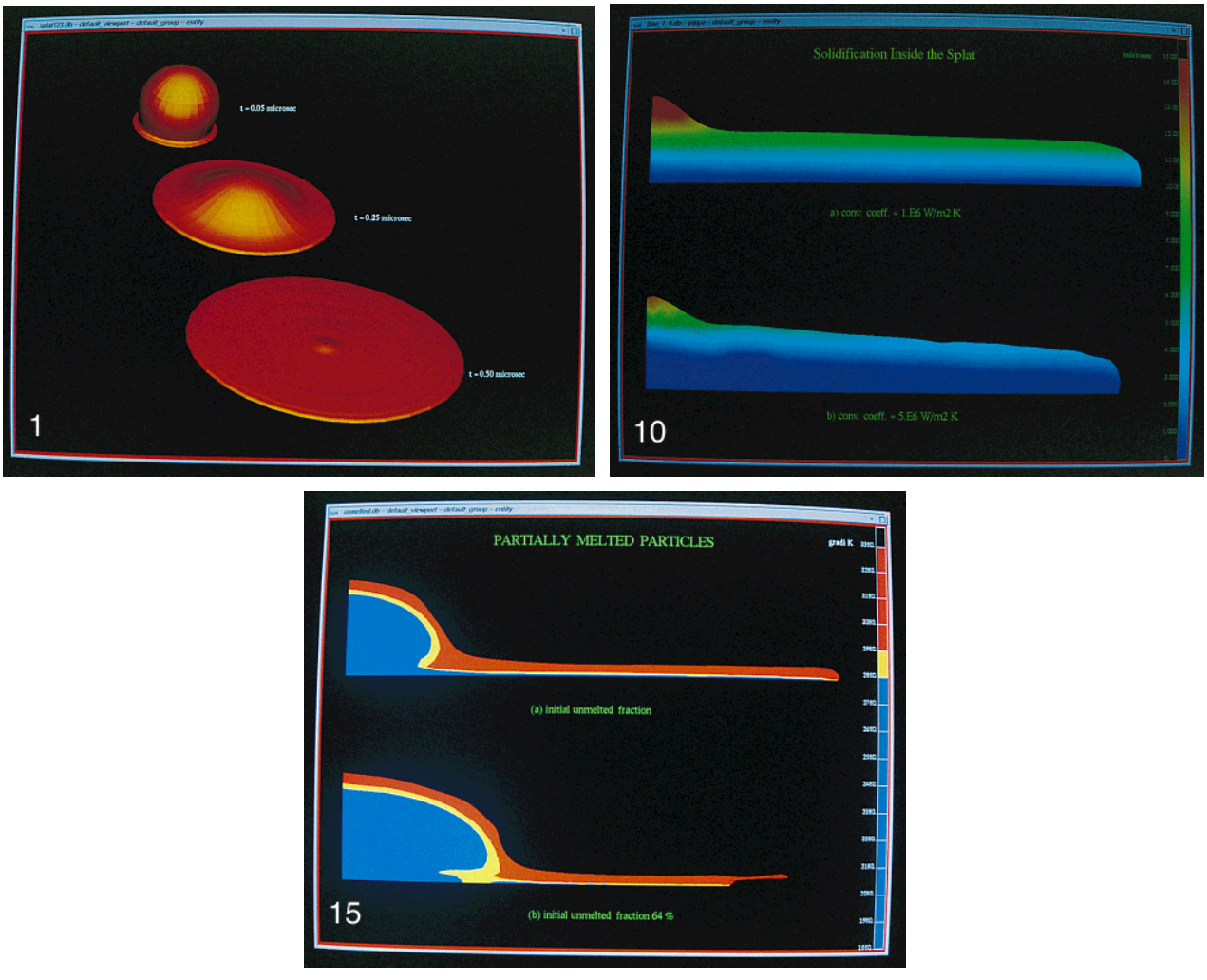

FIG. 1. Evolution of a simulated impact process.

FIG. 10. Progress of solidification front inside the splat (time in μs): Top, $\alpha_c = 1 \times 10^6$ W/m^2 K (case n = 5 of Table III); bottom, $\alpha_c = 5 \times 10^6$ W/m^2 K (case n = 9 of Table III).

FIG. 15. Partially melted particles: Top, 83% melted; bottom, 36% melted (dark, unmelted; light, liquid).

microstructure and therefore to its thermal and mechanical properties. In this connection, the impacting sequence of droplets is important as investigated in [14].

In reviewing previous modelling work on the subject one of the most far reaching, although simplified, approaches, is due to Madejski [17] that investigated the impingement and solidification of liquid droplets both theoretically and numerically. He made four main assumptions: first, that the kinetic energy of the particle goes completely into viscous dissipation and changes in surface energy due to the change of shape; second, that the particle deforms to a thin disk; third, that heat flow is everywhere normal to the surface; fourth, that the velocity field is the simplest one satisfying the continuity equation. The model predicts asymptotic values for the spreading degree $\xi = D/d$ (i.e., the ratio of the final disc diameter, D, to that of the original particle, d) of the impacting particles for different cases (degree of solidification, Reynolds number, and Weber number). If it is further assumed that solidification can be ignored, a simple equation for the spreading degree ξ may then be obtained,

$$\frac{3\xi^2}{\mathscr{W}} + \frac{1}{\mathscr{R}}\left(\frac{\xi}{1.2941}\right)^5 = 1, \tag{1}$$

provided that the Reynolds number, $\mathscr{R} = \rho V d/\mu$, is greater than 100. In (1), $\mathscr{W} = \rho V^2 d/\sigma$ is the Weber number, and ρ, V, d, μ, and σ are the density, velocity, diameter, viscosity, and surface tension of the droplet. McPherson [5] has

TABLE I

Process Parameters and Material Data

Process parameters			
Particle diameter, d	20 ÷ 40	(20)	μm
Particle velocity at impact, V	120 ÷ 180	(180)	m/s
Initial particle temperature, T_o	3200 ÷ 3400	(3400)	K
Material data			
Density, ρ	5.55×10^3		Kg/m^3
Specific heat, c	500 ÷ 1000	(500)	J/Kg K
Thermal conductivity, λ	2		W/m K
Latent heat of solidification, q_L	6.1×10^5		J/K
Solidus temperature, T_S	2680 ÷ 2880	(2880)	K
Liquidus temperature, T_L	2700 ÷ 2980	(2980)	K
Viscosity at 3200 K, μ	4.2 ÷ 42	(42)	mPa s

pointed out that for plasma spraying the term $3\xi^2/\mathscr{W}$ is negligible. With reference to Table I, the Weber number within our range of interest is between 3000 and 15000. Accordingly, the first term in Eq. (1) is approximately 30 to 50 times lesser than the second term. We thus obtain

$$\xi = D/d = M\mathscr{R}^{0.2} = M\left(\frac{\rho V d}{\mu}\right)^{0.2}, \tag{2}$$

where M is a constant coefficient equal to 1.2941 in Madejski's analysis. For Reynolds numbers less than 100, $\mathscr{R}$ should be replaced by $\mathscr{R} + 0.9517$. This formula has been examined both experimentally and numerically; results indicate that it tends to overestimate the measured final diameter [10–12, 18].

A different approach has been developed using shock theory by Houben [19, 20] and the morphological characteristics of the final shape of the splats have been deduced. In this regard it is not clear if a shock wave approach is fully legitimate in treating impacts in thermal spraying since the Mach numbers involved are low (0.05 or less) as pointed out by Trapaga and Szekely [10]. Moreover, this particular theory does not explicitly relate final geometry and initial conditions, i.e., the relevant information needed in models of the deposition process.

A completely numerical approach has been followed by Trapaga *et al.* [10, 11], where both fluid flow and thermal phenomena have been considered. The fluid flow and thermal governing equations are there solved within a finite difference formulation and implementation referring to an Eulerian description of motion. In [12] Yoschida *et al.* presented also a numerical simulation of impacting droplets based on a variant of the marker-and-cell technique (MAC) for the solution of the Navier–Stokes equations for moving free surfaces. A finite element approach was developed by Fukai *et al.* in [13] for the very purpose of the axisymmetric deformation of liquid droplets during impact. In contrast to previous models, their formulation refers to the Lagrangean description of material motion and is combined to mesh generation in order to cope with extensive deformation in the melt. The study covers a wide spectrum of parameters indicating the significance of both surface tension and viscosity. Accordingly, reference to the pertinent literature on the subject is extensive in [13]. One might add to this list the highly interesting numerical investigation by Foote [21] which deals with the dynamics of collision of water droplets, sensitive to the Weber number and therefore beyond the scope of our present investigation.

Independently of the specific developments of [13], here the investigations of the splashing of melted ceramic droplets are based on a utilization of the general purpose Finite Element Programming System FEPS, developed at the Institute for Computer Applications (ICA). An early description of this research software is given in [34]. For the purpose of the present study, a nonlinear finite element procedure has been compiled from the advanced library of the FEPS system in order to model appropriately the physical phenomena involved. We gave preference to the Lagrangean branch of the software. Thereby the dynamic motion of the viscous melt in the drops as constrained by surface tension and the developing contact with the substrate, is ultimately coupled to transient thermal phenomena. Friction phenomena as well as thermal phenomena, accounting also for the solidification of the material, were conveniently implemented in the finite element approach.

The organization of the article is as follows. First the description of the mathematical and numerical formulation of the problem to be modelled is summarized in Section 2. A discussion on the relevant input parameters and boundary conditions of the model follows in Section 3. Results for complete simulations of impact processes and sensitivity studies on the variation of process parameters are reported in detail in Section 4. In the subsequent discussion of the results the utilization of the proposed model in correlating spreading degrees with the initial process parameters is indicated. The latter issue is required as an input for modelling the material deposition.

2. NUMERICAL FORMULATION

2.1. *Impact Motion*

In view of the discretization of the impact problem by finite elements, we propose the weak form of the momentum balance for a volume element V bounded by the surface S,

$$\int_V (\rho \tilde{\mathbf{v}}^t \dot{\mathbf{v}} + \tilde{\boldsymbol{\delta}}^t \boldsymbol{\sigma})\, dV = \int_V \tilde{\mathbf{v}}^t \mathbf{f}\, dV + \int_S \tilde{\mathbf{v}}^t \mathbf{t}\, dS. \tag{3}$$

In (3), ρ denotes the density of the medium, $\mathbf{v}$ is the 3×1 velocity vector and $\boldsymbol{\sigma}$ is a 6×1 array comprising

the independent components of the Cauchy stress: $\boldsymbol{\sigma} = \{\sigma_{xx}\sigma_{yy}\sigma_{zz}\sqrt{2}\sigma_{xy}\sqrt{2}\sigma_{yz}\sqrt{2}\sigma_{xz}\}$. Also, the body force vector acting per unit volume is denoted by $\mathbf{f}$; the vector of surface traction per unit surface is denoted by $\mathbf{t}$. The symbols $\tilde{\mathbf{v}}$ and $\tilde{\boldsymbol{\delta}}$ stand for a virtual velocity field and the associated rate of deformation, respectively. The latter is represented by a 6×1 vector array based on the symmetric part of the velocity gradient: $\boldsymbol{\delta} = \{\delta_{xx}\delta_{yy}\delta_{zz}\sqrt{2}\delta_{xy}\sqrt{2}\delta_{yz}\sqrt{2}\delta_{xz}\}$.

The specification of the inertia term in (3) depends on the choice of the reference system for the motion of the material. It is expected that large deformations of the medium may deteriorate a computational mesh which follows completely the material motion (Lagrangean approach). On the other hand, a computational mesh fixed in space (Eulerian approach) seems not suitable for the description of the motion of the bounding surface. For the above reasons we indicate ab initio the possibility of an independent motion of the reference system characterized by the local velocity $\mathbf{w}(\mathbf{x}, t)$. In this case the acceleration of material particles in (3) is expressed by

$$\dot{\mathbf{v}} = \frac{\partial \mathbf{v}}{\partial t} + \frac{\partial \mathbf{v}}{\partial \mathbf{x}}[\mathbf{v} - \mathbf{w}]. \tag{4}$$

The first term in (4) represents the acceleration at the location considered, the second, convective term depends on the velocity $\mathbf{w}$ of the motion of that location, as compared to the particle velocity $\mathbf{v}$ there. For $\mathbf{w} = \mathbf{v}$ the reference system follows the motion of the material and the convection term vanishes, whilst $\mathbf{w} = \mathbf{0}$ refers to a system fixed in space.

In the finite element methodology the velocity field is approximated within each finite element by

$$\mathbf{v} = \boldsymbol{\omega}_e \mathbf{V}_e, \tag{5}$$

where the $3n \times 1$ vector $\mathbf{V}_e$ comprises the velocities of the n element nodal points and the matrix $\boldsymbol{\omega}$ contains the interpolation functions. The rate of deformation may be derived from (5) in the form

$$\boldsymbol{\delta} = a_e \mathbf{V}_e, \tag{6}$$

with the matrix a_e representing the customary small strain operator obtained from the element kinematics at the actually deformed state.

Also, the velocities at the nodal points of individual elements are extracted from the $3N \times 1$ array $\mathbf{V}$ collecting the velocities at the N nodal points of the finite element mesh. This operation may be symbolized by

$$\mathbf{V}_e = \mathbf{a}_e \mathbf{V}. \tag{7}$$

Introducing next the finite element approximation in (3), we obtain the equations of motion for the discretized system in the matrix form [22]:

$$\mathbf{M}\dot{\mathbf{V}} + \mathbf{N}[\mathbf{V} - \mathbf{W}] + \mathbf{S} = \mathbf{R}. \tag{8}$$

In (8), $\mathbf{M}$ denotes the mass matrix of the system and $\mathbf{N}$ is the convective matrix. The vector array $\mathbf{W}$ comprises the velocities of the nodal points which may be moved independently of the material particles temporarily occupying the same locations (velocity $\mathbf{V}$). The vector $\mathbf{S}$ collects the resultants of the internal stresses at the mesh nodal points, $\mathbf{R}$ represents the discretized external forces.

For typographical brevity we detail in the following the transition from the continuum (cf. (3)) to the discretized system as represented by (8) only for the stress term. Utilization of the finite element kinematics for the stress term in (3) yields the volume integral for an individual element

$$\int_{V_e} \tilde{\boldsymbol{\delta}}^t \boldsymbol{\sigma}\, dV = \tilde{\mathbf{V}}_e^t \left[\int_{V_e} a_e^t \boldsymbol{\sigma}\, dV \right] = \tilde{\mathbf{V}}_e^t \mathbf{P}_e. \tag{9}$$

Accordingly, the vector array $\mathbf{P}_e$ comprises the resultants of the element stress $\boldsymbol{\sigma}$ at the nodal points. The extension to the integral over the entire discretized domain is effected by summation of all element contributions (9) and may be symbolized by the matrix operation

$$\int_V \tilde{\boldsymbol{\delta}}^t \boldsymbol{\sigma}\, dV = \{\tilde{\mathbf{V}}_e\}^t \{\mathbf{P}_e\} = \tilde{\mathbf{V}}^t \mathbf{S}. \tag{10}$$

The stress resultants at the mesh nodal points,

$$\mathbf{S} = \{\mathbf{a}_e\}^t \{\mathbf{P}_e\} = \mathbf{a}^t \mathbf{P}, \tag{11}$$

are thus obtained with the element contributions $\mathbf{P}_e$ as from (9). The computation of $\mathbf{P}_e$ is based on an evaluation of the volume integral for the stress $\boldsymbol{\sigma}$ at the actual geometry of the element. The latter is a result of the motion of the discretization mesh with the velocity $\mathbf{W}$.

For the viscous isochoric medium considered here, the deviatoric part of the stress is related to the rate of deformation by the viscosity coefficient μ:

$$\boldsymbol{\sigma}_D = 2\mu \boldsymbol{\delta}_D. \tag{12}$$

Also, a relaxed isochoric condition is used and relates the hydrostatic stress to a negligible volumetric rate of deformation

$$\sigma_H = 3\bar{\kappa}\delta_V \tag{13}$$

via the numerical penalty factor $\bar{\kappa} \to \infty$.

The element stress resultants $\mathbf{P}_e$ as in (9) then become

$$\mathbf{P}_e = \left[\int_{V_e} a_e^t \boldsymbol{\mu} a_e \, dV\right] \mathbf{V}_e \tag{14}$$

and, although the material viscosity matrix $\boldsymbol{\mu}$ collectively represents both (12) and (13), evaluation for the hydrostatic part of the volume integral is performed to a lower approximation than for the deviatoric part in order to avoid overconstraint by the isochoric condition. With (14), the stress resultants at the mesh nodal points in (11) may be expressed in terms of the nodal point velocities by

$$\mathbf{S} = \overline{\mathbf{D}}\mathbf{V}, \tag{15}$$

where $\overline{\mathbf{D}}$ represents the viscosity matrix of the discretized system as referring to the penalty approach to the isochoric condition.

We return to the finite element equation of motion, (8), which is an ordinary differential equation for the velocity, and obtain a fully algebraic equation by linking velocity and acceleration via an approximate integration within a time increment $\tau = {}^b t - {}^a t$. The following implicit approximation scheme is based on the acceleration ${}^b\dot{\mathbf{V}}$ at the end of the time increment under consideration. It furnishes the velocity,

$${}^b\mathbf{V} = {}^a\mathbf{V} + \tau[a\,{}^a\dot{\mathbf{V}} + b\,{}^b\dot{\mathbf{V}}] \tag{16}$$

and the nodal point positions

$${}^b\mathbf{X} = {}^a\mathbf{X} + \tau\,{}^a\mathbf{V} + \tau^2[c\,{}^a\dot{\mathbf{V}} + d\,{}^b\dot{\mathbf{V}}] \tag{17}$$

at time instant ${}^b t$ at the end of the increment which are necessary in order to obtain the geometry of the discretization mesh if this is chosen to follow the motion of the material. The parameters *a, b, c, d* in (16) and (17) control the numerical performance of the integration and may be adapted to particular time stepping schemes known in the literature.

The system (8) which may be nonlinear in the velocity is solved for $\mathbf{V} = {}^b\mathbf{V}$ at time instant $t = {}^b t$ via the recurrence formula

$$\mathbf{V}_{i+1} = \mathbf{V}_i + \mathbf{H}_i^M\{\mathbf{R} - \mathbf{S} - \mathbf{N}[\mathbf{V} - \mathbf{W}] - \mathbf{M}\dot{\mathbf{V}}\}_i \tag{18}$$

and furnishes the result of iteration $i + 1$ using the data obtained in the ith iteration cycle. The best choice for the iteration matrix $\mathbf{H}^M$ is based on the inverse of the gradient of the residuum within the brackets in (18) with respect to $\mathbf{V}$. For convenience, the gradient is approximated by the expression

$$\mathbf{G}^M \Leftarrow -\left[\overline{\mathbf{D}} + \frac{1}{\tau b}\mathbf{M}\right] \tag{19}$$

which considers the inertia term and accounts merely for a linear dependence of the stress resultants on the velocity, whilst the nonsymmetric contribution from the convective term is avoided as is also a possible dependence of the applied forces on the kinematics of the deformation.

When points on the surface of the medium contact the target, contact forces $\mathbf{F}_n$ normal to the surface and friction forces $\mathbf{F}_t$ tangential to it are accounted for in the model via the expressions [23]

$$\mathbf{F}_n = -k_n\mathbf{v}_n \tag{20}$$

and

$$\mathbf{F}_t = -k_t\mathbf{v}_t. \tag{21}$$

Since the material velocity $\mathbf{v}_n$ normal to the surface of the target must be suppressed upon contact, $k_n \to \infty$ represents a penalty factor associated with a relaxed contact condition. The factor

$$k_t = |\mathbf{F}_t|/|\mathbf{v}_t| \le k_{\max} \tag{22}$$

in the above kinematic formulation of a friction force opposed to the tangential velocity $\mathbf{v}_t$, does not restrict the friction law for $|\mathbf{F}_t|$. As an example, for the Coulomb law we have $|\mathbf{F}_t| \le c_f|\mathbf{F}_n|$ in (22) and c_f is the friction coefficient. The limitation by $k_{\max}$ corresponds to a penalty approach to the condition of sticking.

The contact reactions act on the medium in addition to the applied forces. The complete kinematic description of the contact forces by (20), (21) in conformity with the viscous nature of the deformation problem, however, suggests rather a modification of the stress resultants in the system by

$$\mathbf{S} - \mathbf{F} = [\overline{\mathbf{D}} + \mathbf{K}]\mathbf{V} \tag{23}$$

and, accordingly, of the system matrix in (19). In (23), $\mathbf{K}$ denotes a diagonal hypermatrix accounting for the joint action of $\mathbf{F}_n$ and $\mathbf{F}_t$ at the nodal points currently in contact with the target. Thereby the structure of the system matrix $\overline{\mathbf{D}}$ is not affected by the variation of the boundary conditions during the course of the impact. This fact facilitates considerably the computation.

2.2. *Thermal Phenomena*

During impact, intense thermal phenomena occur which are significant for the deformation of the impacting liquid on account of a temperature-dependent viscosity coefficient, for the process of solidification and for the formation of the microstructure. The transient temperature field $T(\mathbf{x}, t)$ in the medium is governed by the balance of energy which may be stated in a weak form as follows:

$$\int_V \left[\tilde{T}(\rho c \dot{T}) + \frac{\partial \tilde{T}}{\partial \mathbf{x}} \left(\lambda \frac{\partial \tilde{T}}{\partial \mathbf{x}} \right) \right] dV = - \int_S \tilde{T} \alpha (T - T_\infty)\, dS + \int_V \tilde{T} \boldsymbol{\sigma}^t \boldsymbol{\delta}\, dV. \tag{24}$$

In (24), c denotes the specific heat capacity of the medium, λ is the thermal conductivity, and α is the heat transfer coefficient. The reference ambient temperature is denoted by T_∞, $\tilde{T}$ represents a virtual temperature field. The first term in the volume integral on the left-hand side of (24) accounts for the rate of change of the internal energy in the medium; the second accounts for the heat exchange in the interior via conduction. On the right-hand side of (24) we then have the heat transfer through the surface of the medium and the heat generated in the interior by the dissipation of mechanical work during the viscous deformation. All the integrals and gradients in (24) are to be evaluated in the actual geometry at the considered time instant.

Following the same approach for the description of the thermal problem as in the mechanical case we may write the time rate of the temperature in analogy to (4) as

$$\dot{T} = \frac{\partial T}{\partial t} + \frac{\partial T}{\partial \mathbf{x}} [\mathbf{v} - \mathbf{w}]. \tag{25}$$

Then, an approximation of the temperature field within each finite element by a suitable interpretation of (5) and application of the formalism outlined in Section 2.1 furnishes the finite element expression of (24). Ultimately, one obtains the matrix equation governing the discretized thermal problem as

$$\mathbf{C}\dot{\mathbf{T}} + \mathbf{K}\mathbf{T} + \mathbf{L}\mathbf{T} = \dot{\mathbf{Q}} \tag{26}$$

(cf. [22]) in which $\mathbf{T}$, $\dot{\mathbf{T}}$ are vector arrays comprising the temperatures and their time rates at the nodes of the finite element mesh, and $\dot{\mathbf{Q}}$ accumulates the heat loading at the nodal points. The latter reflects the rate of mechanical dissipation on the one hand and part of the heat transfer through the surface on the other hand. The matrices $\mathbf{C}$, $\mathbf{K}$, $\mathbf{L}$ represent the heat capacity, convection, and conductivity of the system, respectively. The convection matrix $\mathbf{K}$ goes back to the second term of expression (25) for the time rate of the particle temperature and vanishes in a Lagrangean description of the problem in which the reference system moves together with the material ($\mathbf{w} \equiv \mathbf{v}$). The conductivity matrix $\mathbf{L}$ comprises, in addition, that part of the heat transfer through the surface which depends on the actual temperature.

At this place we remark for completeness, that in order to account for solidification, the associated latent heat effect is modelled by a suitable modification of the specific heat capacity in the matrix $\mathbf{C}$ within the temperature interval specifying the change from the liquid to the solid phase. In particular, denoting by T_L and T_S the liquidus and the solidus temperatures, respectively, we may define the modified specific heat capacity as

$$c^* = c + q_\mathrm{L}/(T_\mathrm{L} - T_\mathrm{S}), \tag{27}$$

where q_L is the latent heat appertaining to the solidification process.

The definition of the apparent heat capacity c^* in (27) supplies the enthalpy change $\int c^*\, dT$ for the transition from T_L to T_S. The approach is applicable as long as the interval $(T_\mathrm{L} - T_\mathrm{S})$ is finite. In the case of pure materials the phase changes at a specified temperature; hence the temperature interval in (27) is then a numerical artifact. In this connection, we found previously that diminishing the temperature interval affects the transient process but not the ultimate stationary solution in fixed-flow domains. The situation might be different if phase change occurs concurrently with mechanical deformation.

A fully algebraic equation for the thermal problem is obtained by linking in (26) the temperature and its time rate within a time increment $\tau = {}^b t - {}^a t$ by the approximate time integration scheme

$${}^b\mathbf{T} = {}^a\mathbf{T} + (1 - \zeta)\tau\, {}^a\dot{\mathbf{T}} + \zeta\tau\, {}^b\dot{\mathbf{T}}, \tag{28}$$

where

$$0 \le \zeta \le 1 \tag{29}$$

is a collocation parameter. At a fixed state of motion, the solution of the system (26) in conjunction with (28) may then be performed for the time rate $\dot{\mathbf{T}} = {}^b\dot{\mathbf{T}}$ of the temperature at time instant $t = {}^b t$ in analogy to (18) by the iteration

$$\dot{\mathbf{T}}_{i+1} = \dot{\mathbf{T}}_i + \mathbf{H}_i^T [\dot{\mathbf{Q}} - \mathbf{C}\dot{\mathbf{T}} - \mathbf{K}\mathbf{T} - \mathbf{L}\mathbf{T}]_i. \tag{30}$$

Here, the iteration matrix is taken as

$$\mathbf{H}^T = -[\mathbf{G}^T]^{-1} \tag{31}$$

and

$$\mathbf{G}^T \Leftarrow -\mathbf{C} - \zeta\tau[\mathbf{K} + \mathbf{L}] \tag{32}$$

is a convenient approximation to the gradient of the residuum in the brackets in (30) with respect to the iteration variable $\dot{\mathbf{T}}$.

Since the thermal equation (26) and the mechanical equation (8) interact via the temperature and the deformation, they represent a coupled system. The fully algebraic version of this system implies the approximate time integration schemes (16), (17), and (28) and may be symbolized as

$$\mathbf{F}^M(\mathbf{V}, \dot{\mathbf{T}}) = \mathbf{0}, \quad \mathbf{F}^T(\dot{\mathbf{T}}, \mathbf{V}) = \mathbf{0}. \tag{33}$$

In the numerical computation, the solutions of the above physical subsystems are coupled iteratively. Thereby, the mechanical equations of motion are solved for the velocity at a fixed distribution of temperature and the thermal equations for the temperature rate at a fixed velocity field. The partial solutions may be performed in parallel or in sequence and the results are exchanged accordingly before a new iteration cycle starts for the coupled problem; cf. [24, 25].

2.3. *Modifications of the Finite Element Mesh*

In order to avoid severe distortions of the computation mesh which affect the quality of the numerical solution nodal points may be allowed to move independently of material particles. This was fully accounted for in the formalism of Sections 2.1 and 2.2 so that the solutions for velocity and temperature refer to mesh nodal points with velocity $\mathbf{w}$ different from the particle velocity $\mathbf{v}$ at the same locations. The artificial motion of the computation mesh as based on $\mathbf{w}$ is to be chosen such that quality is maintained despite the distortion of the material. Thereby, bounding surfaces of the material have to be respected which means that for the velocities normal to the surface $\mathbf{w}_n = \mathbf{v}_n$ whilst $\mathbf{w}_t \neq \mathbf{v}_t$ in the tangential direction.

The expressions appearing in the equations governing impact motion and transient temperature because of the artificial motion of the reference system are nonsymmetric and inherently nonlinear and cause computational inconvenience. It may therefore be preferable to solve at each time instant a Lagrangean problem first for which the computational mesh follows the material motion and to perform the artificial motion of the mesh nodal points subsequently whilst particle positions remain fixed in space. Reference of the solution to the computation mesh may then be based on the convective expressions (4) and (25) as

$$\frac{\partial \mathbf{v}}{\partial t} = \dot{\mathbf{v}} + \frac{\partial \mathbf{v}}{\partial \mathbf{x}}[\mathbf{w} - \mathbf{v}], \quad \frac{\partial T}{\partial t} = \dot{T} + \frac{\partial T}{\partial \mathbf{x}}[\mathbf{w} - \mathbf{v}], \tag{34}$$

where $\dot{\mathbf{v}}$, $\dot{T}$ refer to material particles with velocity $\mathbf{v}$ and $\partial\mathbf{v}/\partial t$, $\partial T/\partial$t to mesh positions moving with velocity $\mathbf{w}$. Still, the spatial gradients required in (34) represent a critical issue for discretized solutions. Furthermore, an incremental technique based on (34) is restricted to small displacements of the mesh relative to the material and therefore implies a continuous modification of the mesh in the course of the computation.

Alternatively, the obtained Lagrangean solution may be referred to an a posteriori modified discretization mesh by means of interpolation. This requires the specification of the nodal point positions of the modified mesh with respect to the actual mesh for which the solution was obtained; cf. [23]. Let the nodal point r of the new mesh be contained within the element e of the actual mesh. The solution at r is then obtained in accordance with the finite element approximation from the nodal values of the element. Referring, for instance, to Eq. (5) for the velocities we have

$$\mathbf{v}_r = \boldsymbol{\omega}_e(\mathbf{x}_r)\mathbf{V}_e. \tag{35}$$

The value $\mathbf{v}_r$ at new nodal point r is determined by an evaluation of the interpolation for its position $\mathbf{x}_r$. The above technique is not based on a continuous variation of the nodal point positions and thus allows for occasional modifications of the mesh. Furthermore, the number of nodal points in two consecutive meshes may be different, so that the mesh or parts of it can be completely regenerated if neccessary.

Up to now, we were concerned with the presentation of the numerical solution of the thermomechanically coupled impact problem with reference to a computational mesh deforming independently from the material. The artificial deformation of the discretization mesh, however, has to be steered such that the quality of the numerical solution is maintained throughout the computation despite any unfavourable deformations of the material. To this purpose an improved position $\mathbf{x}_r$ of nodal point r may be determined by

$$\mathbf{x}_r = \sum_{e=1}^{n} w_e \bar{\mathbf{x}}_e \Big/ \sum_{e=1}^{n} w_e. \tag{36}$$

Here, the vector $\bar{\mathbf{x}}_e$ comprises the coordinates of the centre of gravity of element e, w_e is a suitable weighting factor, and summation extends over all elements connected to node r. The effect of (36) is a balancing of the weighting factor among the elements surrounding the nodal point. The weighting factor may be chosen in accordance to an error criterion for the numerical solution [24] or it may be of geometric origin. If based on the volume of the elements, for instance, activation of (36) produces finite elements approaching ideal geometrical shape and with smooth tran-

sition of size within the mesh. Instruction (36) for the modification of nodal point positions is equally applicable to the improvement of the mechanical or the thermal solution, depending on the choice of the error criterion. In particular, nodal points might follow the propagation of the solidification front.

Under certain circumstances, the above modification procedure may be not sufficient and a complete or partial regeneration of the discretization mesh is then required. To this end an automatic mesh generation algorithm [26] has been modified for activation during the course of the numerical simulation [27]. The original algorithm performs an automatic generation of the finite element mesh on the basis of blocks and mean element sizes defined by the user, the specification of refinement regions and factors. Its utilization for mesh regeneration during computation is straightforward, the transfer of the numerical solution to the new mesh follows the interpolation procedure described previously.

3. PROCESS PARAMETERS, MATERIAL DATA, AND BOUNDARY CONDITIONS

Although the relevant primary process parameters for plasma spraying (like voltage settings, current intensity substrate temperature) are well known, the detailed information needed in our numerical analysis of ceramic droplets (for example, particle temperature and velocity inside the flame and particle material properties) is nevertheless not generally available.

In the present study we have used a single set of process parameters investigated experimentally and discussed by Vardelle *et al.* [28] for the case of thermal spraying of yttria stabilized zirconia (8% wt Y_2O_3). In particular, in the following simulations, we have relied on the reported measurements of particle size, impact velocity, and in-flight particle surface temperature distributions for the aforementioned ceramic powder. Table I collects the range of process parameters and material data that have been considered in the numerical studies; numbers in brackets indicate the values used in our reference case.

Material data for fused and sprayed zirconia are extremely variable, and only reasonable average values can be usefully extracted from the literature. The viscosity is perhaps the most critical material parameter to assess. We have made use of the following temperature dependence deduced by a scaling procedure proposed by Harding [30] and based on the experimental measurements of the viscosity of a structurally similar oxide (namely, UO_2, from Fink *et al.* [31]),

$$\mu = A \exp\left(\frac{4620}{T}\right), \tag{37}$$

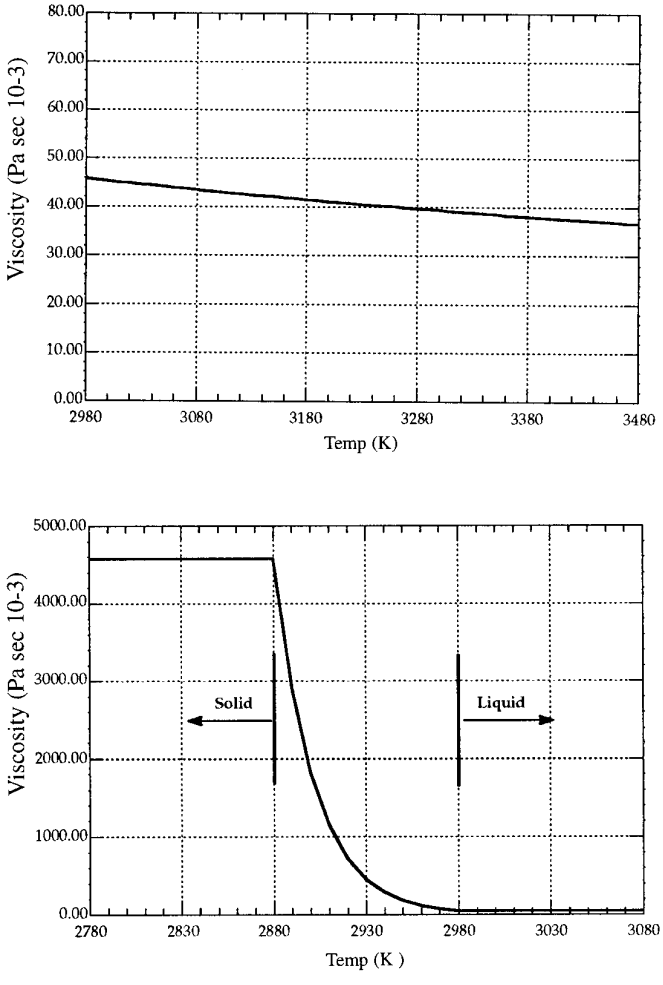

FIG. 2. Variation of viscosity with temperature: top, liquid state; bottom, range between solid and liquid phases.

where T is the temperature in K, μ is the viscosity in mPa s, and A is a coefficient that remains to be determined for the zirconia material. With references to Table I we obtain from (37) for $\mu = 42$ mPa s at $T = 3200$K, the value $A = 9.70$. The viscosity increases as temperature decreases following (37) up to the liquidus solidification temperature as shown in Fig. 2, top for $A = 9.70$. Then, its value is increased (rapidly, but smoothly, following an exponential functional dependence within the range between the liquidus and solidus temperatures) by orders of magnitude to simulate the stiffness of the solid material (see Fig. 2, bottom).

Another important physical property that depends strongly on the spraying conditions is the temperature field inside the particle at the instant of impact. Torch characteristics, gas velocity and composition, particle granulometry, and trajectory inside the flame influence heat flow to and from the particle (see, for example, Vardelle *et al.* [2]). During its flight the particle experiences a rapid and violent

initial heating followed by a cooling down at the surface as it exits the flame [33]. Thus, depending on the particular spraying conditions, the final temperature field can be either very uniform or unmelted zones can be present inside the particle, with temperature variations of the order of hundreds of degrees. In a first investigation we have considered completely melted particles with a uniform initial temperature T_o equal to the average surface temperature measured experimentally in [18]. Then calculations have been performed to estimate the influence of the presence of unmelted material on the flattening degree.

Thermal and mechanical boundary conditions during impact are indicated in Fig. 3. Thermal boundary conditions comprise heat flow from the droplet to the substrate and to the surrounding gas. The latter is controlled by the radiation emissivity ε of the material interpreted as convective heat transfer in conjunction with a temperature-dependent heat transfer coefficient and was found to give a minor contribution to the dissipation of heat during the fast spreading and cooling process. The fundamental thermal process is heat flow to the substrate, as will be confirmed in the present study. In particular it is found to be essentially determined by the interface properties; thermal conductivity of zirconia and of substrate material play a minor role, compared to the thermal resistance at the interface. In simplified modelling, heat flow to the substrate was substituted by convective heat transfer with fictitious heat transfer coefficient α_c and reference temperature T_∞. Detailed consideration of the transient thermal conditions in the substrate was thus avoided.

Mechanical boundary conditions imposed in the model are (i) the surface tension σ and (ii) Coulomb friction with friction coefficient c_f upon contact with the substrate. Surface tension is found to have a negligible effect in slowing down the splashing process, compared to viscous dissipation. The contact friction may either cause material points on the surface of the droplet to stick to the substrate or allows them to still slip away. However, simulations have shown that a variation of the friction condition has only an influence on the deformation of the material close to the contact surface, without affecting the final splat shape. We did not consider here the wetting effects on the spreading of the droplet. A combined numerical and experimental investigation of this issue for water droplets may be found in the paper by Fukai *et al.* [32]. The proposed approach requires specific experimental data on the wettability of the substrate as input to the numerical model.

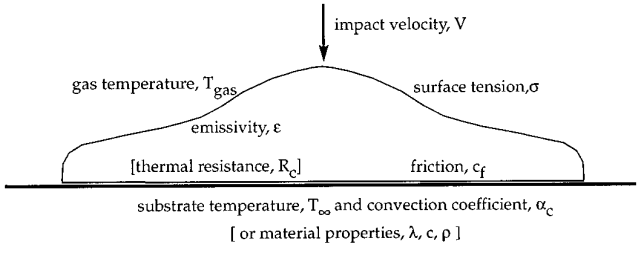

FIG. 3. Boundary conditions.

TABLE II

Thermal and Mechanical Boundary Conditions

Gas temperature, T_G	1200 ÷ 1800	(1800)	K
Substrate temperature, T_∞	400 ÷ 1200	(1200)	K
Radiation emissivity, ε	0.2 ÷ 0.6	(0.4)	
Substrate conv. coef., α_c	1 ÷ 5 × 10^6	(1 × 10^6)	W/m^2K
Surface tension, σ	0.5		J/m^2
Coulomb friction coeff., c_f	0.0 ÷ 0.4	(0.2)	

Table II specifies the range of thermal and mechanical boundary condition parameters investigated in the following numerical studies.

4. APPLICATIONS

4.1. *Description of the Simulation*

The computational methodology outlined in Section 2 is available in the Finite Element Programming System (FEPS) developed at the Institute for Computer Applications. The basic software was described in [34]. The research system comprises software modules for the simulation of fluid flow, deformation of solids, and transient temperature analysis, and it is capable of coupling individual processes. The above concept of multi-physics simulation is being steadily extended. At the present stage, mesh generation, adaptive refinement, and a general description of dynamic contact and friction are available as well. The finite element library allows the handling of two-dimensional and completely three-dimensional problems.

In order to comply with the particular requirements of the present impact problem, an algorithm was compiled as based on the Lagrangean description of the dynamic motion of a deforming viscous medium coupled to the temporal development of the temperature distribution. The local temperature indicates onset and completion of solidification which effects a marked increase of the material viscosity, a function of temperature. The surface tension is imposed as an external loading via surface elements. The evolution of contact with the substrate, assumed to be rigid, is followed during the course of the incremental time-stepping of the impact process. Nodal points of the droplet model contacting the substrate develop normal and tangential forces in accordance to the kinematic (viscous) approach described in Section 2.1. The appearance of se-

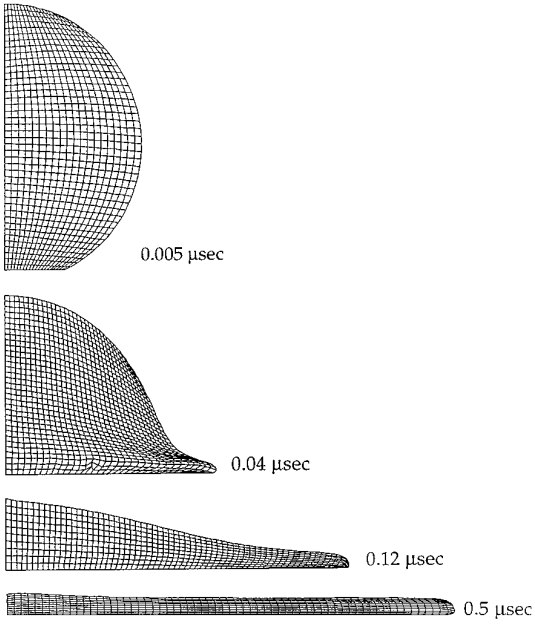

FIG. 4. Adaptable finite element mesh and sequence of deformation.

vere deformations in the Lagrangean mesh during the course of the computation necessitates redefinition of the discretization mesh which is not executed continuously but rather occasionally when certain geometric criteria are met.

In the following, we first present in detail a reference simulation run. It describes the thermomechanically coupled computation of the normal impact of a completely molten spherical particle on a flat, rigid surface. Then we extend the investigations to sensitivity studies on the process parameters and to the case of partially melted particles.

The thermomechanical simulation is performed until the motion of the splat on the surface stops. The thermal calculation is continued further in order to investigate the cooling down process until complete solidification of the splat. Axial symmetry is utilized and decreases the size of the problem. Figure 4 shows the discretization by quadrilateral axisymmetric elements (four nodes), employed for both the mechanical and the thermal phenomena in an initial investigation of the problem, together with a sequence of deformation during impact.

For every impact event the simulation always starts with an initial mesh representing a sphere of given radius, velocity, and temperature distribution at the instant of the impact with the substrate. In preliminary studies a uniform mesh, such as in Fig. 4, was used to investigate the type of deformations present in the process. Two levels of deformation could be recognized: close to the contact region the deformation is local in nature, whilst global deformation introduces pronounced changes in the shape of the droplet free surface. Accordingly, two types of mesh redefinition have been used in the continuation of the simulations:

- a local redefinition of the mesh was applied when the element deformation due to the dynamic motion becomes too high to maintain the quality of the solution. To this purpose, the aspect ratio of the concerned quadrilateral elements was monitored automatically during the simulation. When it exceeded a prescribed value, the computation was interrupted. The mesh was then modified and the calculation was restarted with the new mesh.

- a global redefinition of the mesh was applied when the shape of the droplet free surface was changed drastically by the dynamic motion. In this case the aspect ratio of all quadrilateral elements was monitored automatically during the simulation. In the case of high distortion, the computation was interrupted, the mesh globally regenerated, and the calculation restarted with the new mesh.

In Fig. 4, the deformed mesh at $t = 0.04$ μs is shown prior to local redefinition. The mesh at $t = 0.12$ μs demonstrates the result of global regeneration.

Figure 5 refers to a different computation mesh designed ab initio finer in the region close to the impact front. The top part of the figure shows a typical deformed mesh at a local critical stage where the computation had to be halted because of extensive local distortion. Figure 5 (bottom) provides a detail of the region where the distortion reached a maximum (almost always in the vicinity of a node coming in contact with the substrate).

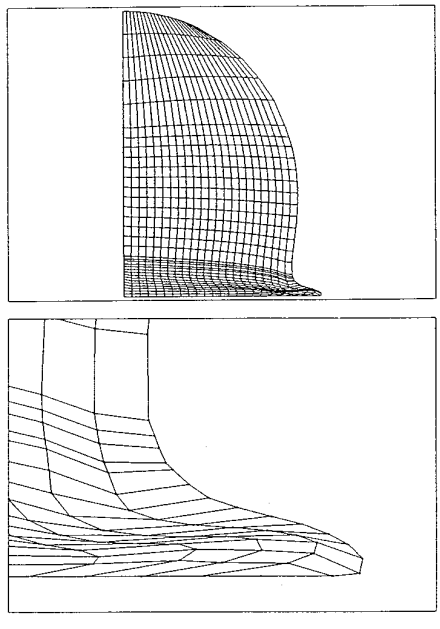

FIG. 5. Example of deformed mesh at a critical stage: top, complete mesh; bottom, detail of the critical region.

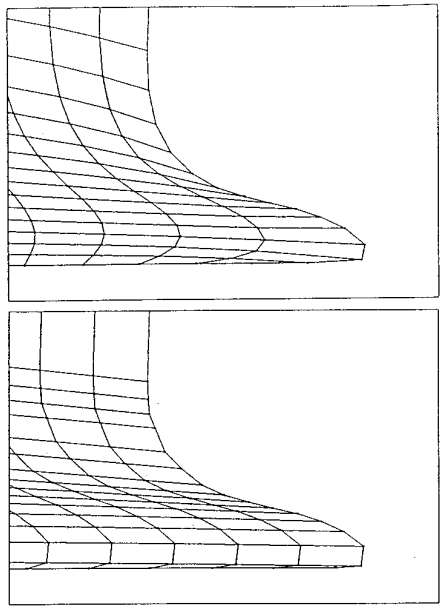

FIG. 6. Details of improved meshes at the critical region: top, smoothing algorithm; bottom, regeneration procedure.

Different techniques to improve the computational mesh have been investigated following the procedures described in Section 2.3. In a first phase we have applied an a posteriori smoothing procedure of the mesh following Eq. (36). The weighting factor was chosen in this case to be the unity, attempting to produce finite elements with best geometrical shape and smooth variation of size within the mesh. This approach succeeds in providing an improved mesh; see the details of the smoothed critical area in Fig. 6 (top), but the degeneration to a triangle of the element affected by the new contact is not removed. Since this problem is inherent to the above smoothing technique, at least a partial regeneration of the mesh is required and its result for the present case is shown in Fig. 6 (bottom). The following results refer to computations based on an automatic mesh regeneration algorithm [26].

To define the reference case-study of the impact, average values of the parameters have been selected from available sets of measurements. The latter were performed under controlled conditions on single splashing events of plasma sprayed zirconia particles at the University of Limoges [8, 29, 28]. The parameters specifying the reference case are indicated in brackets in Tables I and II.

A typical splat evolution is shown both in Fig. 1, where a 3D representation of the axisymmetric 2D computation is shown, and in Fig. 4, where the actual 2D discretization and subsequent mesh deformation are depicted. The remeshing procedure, coupled to an automatic timestep control available in FEPS, allowed thermomechanical calculations of the splash up to the completion of the impact process. Typical computations extend over 10,000 time steps for axisymmetric meshes of 600 to 1000 elements. Normally 30 to 45 mesh regenerations were needed and the necessary CPU time on a VAXstation 4000 computer was between 30 to 40 h.

The thermal and mechanical evolution is independent of the size of the initial mesh and of the subsequent refinement if a sufficient number of element is used ($\geq$500). We considered the motion of the splashing to be completed when the kinetic energy of the splat fell below 10^{-4} times the initial value. A single problem configuration was followed further and confirmed the validity of the above assumption.

4.2. *Results and Sensitivity Studies for Completely Melted Particles*

Table III collects initial data (particle diameter d, velocity V, and the related Reynolds number $\mathscr{R}$) and outputs results (total splashing time t_s, instant of first appearance of solidification t_{ss}, instant of solidification completion t_{es}, theoretical spreading degree of Madejski's model ξ_M, and computed spreading degree ξ) for a number of simulations performed.

The first part of the table (n = 1 to 6) refers to simulations connected with the investigation of the functional dependence of the spreading degree ξ to the Reynolds number $\mathscr{R}$. The different cases are obtained as variations of droplet diameter and velocity of the reference case (n = 1 in Table III) while all the other parameters remain constant. The second part of the table (n = 7, 8, 9) refers to results obtained at the respective Reynolds number for different thermal conditions, as specified in the text below and in Fig. 8.

TABLE III

Results of Simulations

n	d μm	V m/s	$\mathscr{R}$	t_s μs	t_{ss} μs	t_{es} μs	ξ_M	ξ
1	20	180	476	0.49	0.50	5.90	4.44	3.24
2	20	120	317	0.67	0.51	6.50	4.09	3.01
3	30	150	595	0.45	0.35	12.70	4.64	3.35
4	40	135	714	0.62	0.16	21.00	4.82	3.36
5	40	170	899	0.94	0.18	20.00	5.04	3.50
6	40	180	951	1.08	0.38	13.20	5.10	3.69
7	20	180	476	0.47	0.17	4.30	4.44	3.22
8	30	150	595	0.27	0.27	8.57	4.64	3.25
9	40	170	899	0.14	0.14	13.50	5.04	3.32
10	20	180	4760	—	—	—	—	—

Note. t_s = spreadingtime, t_{ss}, t_{es} = start, end of solidification, ξ_M = spreading degree from Madejski model, ξ = spreading degree from simulations. Simulation number n = 1 is the reference case.

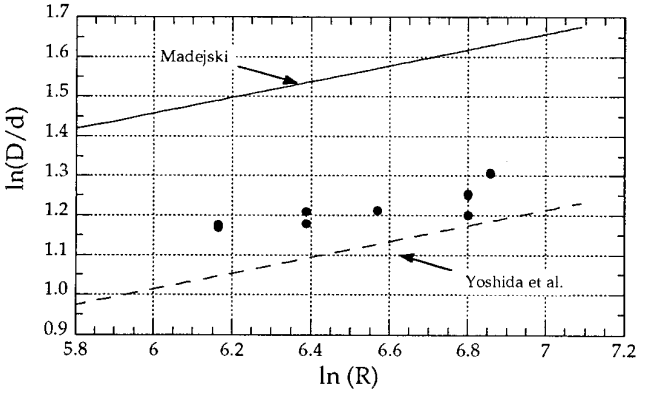

FIG. 7. Spreading degree versus Reynolds number. Black dots are results of the present study.

The last entry in Table III (n = 10) refers to the parameters used in a study of the reference case but with a low viscosity, therefore a high Reynolds number, discussed below and in subsequent figures.

The values of ξ obtained from our model are well below the theoretical predictions of Madejski's model and slightly higher than other numerical estimates (see data from Yoshida *et al.* [12]). Madejski's simple relation (see Eq. (2)) is based on the assumption of a cylindrical deformation of the splat and for the case without solidification. Our model relaxes both the assumptions and the values for the spreading degree are found to be reduced. The data from Yoshida *et al.* [12] refer to a different material, namely Al_2O_3. A comparison among the different data is given in the logarithmic diagram of Fig. 7. An interesting result is that in our model, as in Yoshida's calculations, single spreading results are reasonably fitted by a relation of Madejski's type (see Eq. (2)) by using in the present case a modified coefficient $M = 0.925$:

$$\xi = 0.925\mathscr{R}^{0.2}. \tag{38}$$

The temporal evolution of ξ and its dependence on mechanical and thermal parameters is shown in Fig. 8. Mechanical parameters such as viscosity, initial velocity, and particle diameter (upper frame) have a major influence on the splashing process (see the upper frame of Fig. 8, where cases n = 1, 2, 6, and 10 in Table III are compared). The influence of viscosity on the splashing process is relevant: a low viscosity as expressed in Eq. (37) with $A = 0.97$ corresponds to splats that evolve rather like a liquid than a viscous solid. In Fig. 9 a snapshot of the low viscosity case ($A = 0.97$, case n = 10 in Table III) is compared with a high viscosity model ($A = 9.70$, case n = 1 in Table III) at the same instant. The calculations for the low viscosity cases (as curve (c) in Fig. 8) were interrupted due to the appearance of extensive deformations at the contact sur-

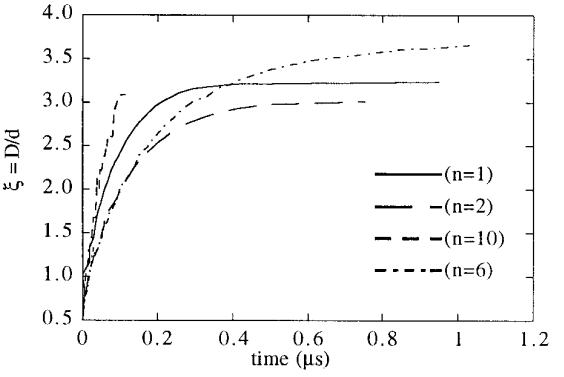

n=1: reference case (see text); n=2: V = 120 m/sec;
n=10: μ = 0.97 exp(4620/T) mPa s; n=6: d = 40 μm;

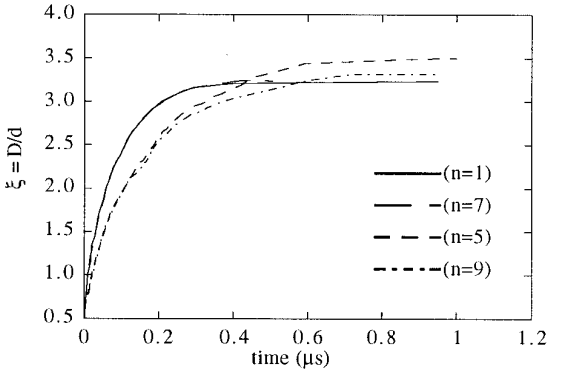

n=1: reference case (see text); n=7: T_∞ = 400 K;
n=5: d =40 μm, V = 170 m/s, T_0 = 3200 K, T_{gas} = 1200 K;
n=9: like n=5, but $\alpha_c = 5 \times 10^6$ W / m^2 K

FIG. 8. Spreading degrees versus time.

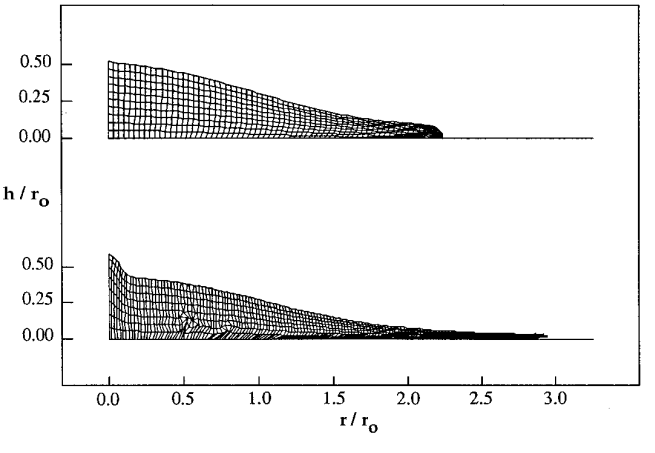

above μ = 9.70 exp (4620/T) (case n = 1 in table 3)
below: μ = 0.97 exp(4620/T) (case n = 10 in table 3)

FIG. 9. Deformed mesh after 0.11 μs.

face, and high deterioration of the mesh in the melt (see Fig. 9). For this range of low viscosity, the redefinition of the mesh has to be performed rather continuously than only occasionally upon the occurrence of a new contact, as done in the high viscosity case. This fact may suggest the use of a combined Eulerian–Lagrangean technique as described in Section 2.3 and requires the definition of an artificial velocity field for the mesh nodal points such that the quality of the discretization mesh can be maintained throughout the flow of the material bounded by the deforming surface of the droplet (cf. [22]). In the following simulations only higher values for the viscosity have been used, since the present model is best suited for these cases.

Thermal parameters such as substrate temperature T_∞, initial droplet temperature T_o, and interface convection coefficient α_c (Fig. 8, bottom frame) are found to have a minor influence on the spreading process but are important for the subsequent cooling and solidification phenomena. In fact, for almost all the parameters considered, temporal scales for splashing and solidification are different (see Table III) and, therefore, these two processes are in fact decoupled. The influence of thermal parameters on the spreading degree is moderate, if they are kept within the experimental range for the specific process. Curves n = 1 and n = 7 of the lower part of Fig. 8, obtained for variations of the substrate temperature from 1200 K to 400 K are essentially superimposed. A change of as much as five times in the interface convection coefficient α_c, as between curve n = 5 and n = 9, causes a variation of about 7% in ξ. A visual assessment of the influence of thermal parameters on ξ can be made directly in Fig. 7, where results for the same Reynolds number, but for different thermal parameters, are also plotted.

On the other hand, the same variation of thermal parameters enhances the overlapping between mechanical evolution and the solidification processes. This fact is demonstrated in Fig. 10, where the development of the solidification front inside the splat is followed for the cases n = 5 and n = 9 of Fig. 8. The time instants at which elements undergo solidification is shown in the contour plot (note that splat shapes have been exaggerated in height by a factor of two to improve data readability). In the case of a high interface convection coefficient (case n = 9) almost half the splat is solidified within 1 μs, i.e., the typical time for the splashing motion. It is interesting to note that, although the presence of solidification during the spreading process influences the final spreading degree, the rapidity of solidification is not so critical; in fact the variation in ξ for the two cases described in Fig. 10 is limited to 7%.

A final evidence of the small influence of material thermal properties in the time range of interest for the spreading process is presented in Fig. 11, where, with reference to the case n = 5, the evolution of the average surface

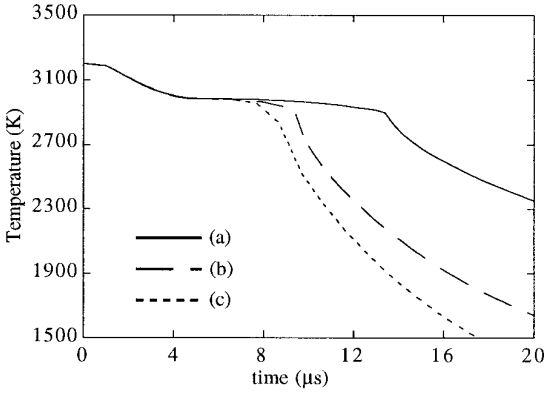

(a) splat on a zirconia substrate; (b) splat on a steel substrate
(c) splat on heat sink

FIG. 11. Temporal evolution of average surface temperature.

temperature is computed for three different substrate model materials. In the first two cases (curves (a) and (b) in Fig. 11) we have extended our model to include also a discretization of the substrate to model conduction to the substrate, while a layer of interface elements (0.2 μm) was used to impose the contact thermal resistance; curve (a) corresponds to a zirconia substrate with thermal conductivity $\lambda_z = 2$ W/mK and contact resistance $R_c = 1/\alpha_c = 1 \times 10^{-}6$ m^{2}K/W; curve (b) corresponds to a steel substrate with thermal conductivity $\lambda_s = 18$ W/mK and the same contact resistance as above. In the third case (curve (c)), the splat is just in contact with a heat sink, like all other simulation of the present account, with a value of the substrate convection coefficient equivalent to the above contact thermal resistance, namely $\alpha_c = 1 \times 10^6$ W/m^{2}K. No differences in cool-down behavior are present for about the first 8 μs. This observation indicates that spreading and cooling down until solidification are little affected by the nature of the substrate. Other parametric studies (see Fig. 10) show the dependence on α_c. The variation of splat emissivity and thermal conductivity inside the particle had practically no effect on cooling down curves and splashing behaviour. These observations enforce the assumption that the cooling of the particle is essentially driven by the interface properties.

4.3. *Results for Partially Melted Particles*

Some computations have been performed to investigate numerically the thermal state of the particles before impact and to explore the possibility of the presence of unmelted material in the droplet at the instant of impact. The temperature fields so obtained have then to be used as starting conditions for the thermomechanical spreading calculations assessing the influence of the presence of ummelted material on the final spreading degree. The issue of partially melted droplets has been considered previously by

San Marchi *et al.* [35] on the basis of a modified Madejski model. The authors assess the range of validity of their approach to be for solid fractions less than 0.40. Therefore, beyond the estimation of the unmelted fraction by the finite element thermal analysis, also investigations of the performance of the present deformation model are justified. Thereby, the presence of unmelted material is simply accounted for by the different values of the parameters for the solid material in the respective region, in particular, the higher value for the viscosity coefficient. The overall computational procedure remains unaltered and is uniquely applied to both the melted and the unmelted parts of the material.

During its flight from the nozzle exit to the impact on the substrate, a ceramic droplet experiences a highly variable external temperature field. At the beginning, as it exits the nozzle, its axial velocity is near zero, and the particle remains in the hottest part of the flame, exposed to temperatures of the order of 15,000 K. After that, as the particle accelerates and travels toward the target, the surrounding flame temperature decreases; if the target is far enough from the flame (and this is the usual condition for the plasma spray process), the surrounding gas temperature becomes lower that the droplet temperature, and the surface temperature of the droplet starts to decrease. Thus, the temperature distribution inside the particle depends on the flame's characteristics as well as on the droplet dimension and the path inside the flame.

Some simplifying assumptions have been made in the following computations: at each time instant the entire surface of the droplet is exposed to the same gas temperature; heat exchange with the surrounding gas is modelled by convection; the path of the droplet is parallel to the flame axis.

To deduce the temporal evolution of the temperature of the gas surrounding the droplet we utilized experimental data and theoretical calculations on flame temperature and particle velocity following Vardelle *et al.* [2]. Flame temperature and particle velocity curves from the cited work are reported in Fig. 12. From droplet velocity and flame temperature curves we deduced the temperatures to which the particle is exposed as a function of the time of flight. These temperature histories were used for the thermal calculations in the heating-up phase; the temporal variation of the gas temperature for a 40 μm diameter droplet traveling along the flame axis and at 3.5 mm from the axis are shown in Fig. 13.

Some calculations have been performed with different values for the temperature in the first part of the particle path. In fact, no data are available on this region of the flame, where the temperature is higher and where the particle spends about half of its flight time due to the low initial velocity.

Different particle sizes and different distances of the particle path from the flame axis have been considered in the transient temperature computation including phase change during flight. Some typical radial temperature profiles at impact for a 40 μm diameter droplet are shown in Fig. 14. Curves refer to the same particle traveling on the flame axis in the presence of different initial flame

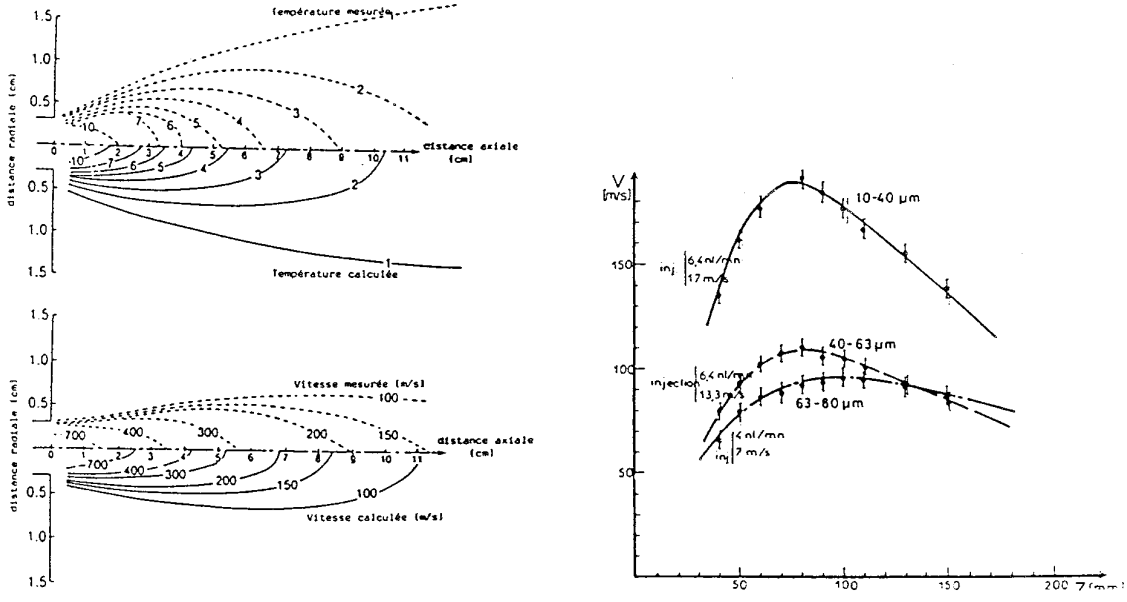

FIG. 12. (Left) Calculated and experimental contours of plasma gas temperature and velocity (plasma gas: Ar − H_2, powder ZrO_2). (Right) Particulate velocity along the plasma jet for the same case. (From [2]).

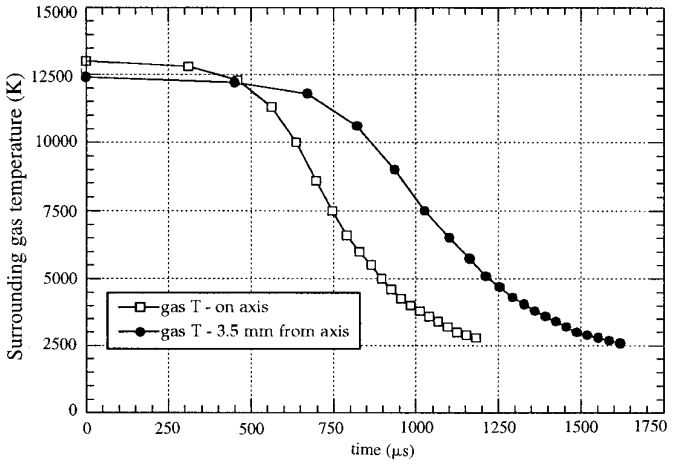

FIG. 13. Gas temperature history at particle for T_{flame} = 13,000 K.

temperatures (namely 11,000, 13,000, and 15,000 K), and for the 13,000 K initial flame temperature, but traveling 3.5 mm from the flame axis. Two characteristic cases can be distinguished:

• particles traveling on the flame axis have a quite uniform radial temperature profile, whatever the initial flame temperature is. Different average temperatures correspond to different initial flame temperatures. The particles are in this case completely melted (or completely unmelted if the flame temperature is too low).

• a different situation arises when the particle is traveling in a distance parallel to the flame axis: in this case the axial temperature variation is high, and the particle is most often only partially melted. For the case described in Fig. 14 about one-half the particle radius is below melting temperature (2880 K for the case considered) at the instant of impact.

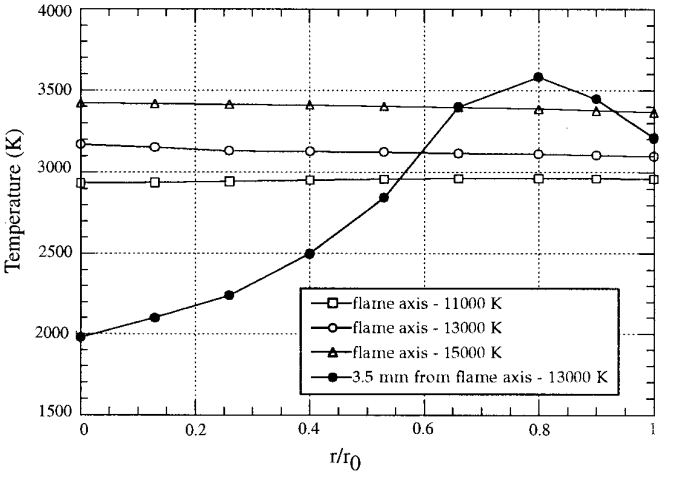

FIG. 14. Radial temperature variation for a 40 μm diameter particle at impact.

Two cases of partially melted particles have been considered for a complete thermomechanical simulation of the spreading process; namely the impacts of 83% and 36% melted particles, maintaining all the other mechanical and thermal parameters as in the reference case of Table III. The initial temperature distributions inside the particles were obtained by appropriate heating-up calculations, following the procedures described above (i.e., proper flight paths out of the flame axis were chosen to provide the required extent of the melted region and the temperature distribution inside the particles). The 83% melted particle has been obtained for the 40 μm diameter droplet of Fig. 14 with 13,000 K initial flame temperature and traveling 3.5 mm from the flame axis. The 36% melted particle has been obtained for a similar case but for a trajectory 7 mm from the flame axis.

The profile of the splats at the end of the spreading is shown in Fig. 15. The dark and light parts represent unmelted and liquid material, respectively. Three observations can be made:

• the unmelted part of the droplet forms in both cases a solid hemiellipsoidal core over which the liquid part flows

• the 36% melted particle develops a jet of material on the outer ring, that can be interpreted as an indication for fragmentation, a fact quite often observed in such impacts in experiments [3]; in this case the calculation was stopped even though the velocities in the jet were still high, because the condition of material fragmentation is not yet part of the numerical algorithm employed.

• very little additional solidification can been observed in the two cases investigated during the period of spreading.

The first observation is in agreement with experimental findings, where looking at the microstructures of plasma-spray coatings, unmelted particles can be seen to form hemispheres (or rather hemiellipsoids) when they hit the substrate.

Other authors (Cirolini *et al.* [16]) developing qualitative models for the spreading process have suggested that the behaviour of a partially melted particle could be represented by the superposition of a completely melted plus a completely unmelted one, each considered independently: the unmelted particle forms a hemisphere (of equivalent volume), over which the melted one spreads, following a Madejski-type relation. A simple model based on the above assumptions is used as a test for the numerical results.

With reference to [16], let us assume that a fraction a of the particle volume is melted, i.e., $V_m = aV$. Then, if we consider the partially melted particle to behave like

TABLE IV

Partially Melted Particles Results

Melted fraction a	Simulation ξ_s	Qualitative model ξ_m
1.00	3.7	3.7
0.83	3.5	3.4
0.36	2.7	2.5

two independent particles, the diameter of these two particles will be respectively $d_m = da^{1/3}$ and $d_u = d(1 - a)^{1/3}$, where d_m is the initial diameter of the melted particle and d_u is the initial diameter of the unmelted particle. Thus, for a completely unmelted particle ($a = 0$) forming a hemisphere of final diameter D,

$$\xi = D/d = 2^{1/3} = 1.26, \tag{39}$$

represents the minimum value for ξ. For a partially melted particle, the melted part is assumed to act as a particle with diameter $d_m = da^{1/3}$; therefore following Eq. (2),

$$\xi_m = D/d = M\left(\frac{\rho V d_m}{\mu}\right)^{0.2}\left(\frac{d_m}{d}\right) = M\left(\frac{\rho V d}{\mu}\right)^{0.2} a^{2/5}. \tag{40}$$

Table IV compares the results of the complete simulation with the simple qualitative model predictions for $M = 0.925$ (see Eq. (38)). The presence of unmelted material in the droplet is found to decrease the spreading degree, and a simple model that assumes a decoupled behaviour for the melted and unmelted parts provides a good quantitative description of the phenomena. It is interesting to note that the present result is in accordance with the quantitative findings of San Marchi *et al.* [35] for the range of validity of their approach, i.e., for solid fractions less than 0.40 that corresponds in our case to value of a between 1.0 and 0.6. As a matter of fact, the same reduction is observed in the spreading degree, and it is confirmed that additional solidification may be regarded a minor effect.

5. CONCLUSIONS

Flow of liquid material, heat-transfer, and solidification phenomena associated with the impingement, spreading, and cooling of high-temperature droplets of zirconia on solid substrates under plasma-spray conditions have been investigated numerically within a finite element approach. The deformation of the splat geometry, as well as the evolution of the thermal field within the splat, have been followed up to the final state. The developed numerical technique utilizes automatic mesh generation procedures. It is appropriate for the range of process parameters considered and is capable of reproducing the main features of experimental findings.

Cases of normal impact of spherical particles (both completely melted or partially melted) on a flat, rigid surface have been studied in detail. The main results of the investigations can be summarized in the following points:

- a clear indication that, for the range of process parameters investigated relative to typical plasma spraying conditions for zirconia powders, two different time scales for mechanical and thermal evolution exist: first, the liquid droplet spreads in a very short time (typically 0.5–1.0 μs); then it continues to cool down and solidifies within 10–20 μs from the beginning of impact.

- the thermal evolution in the splat during and after splashing is in all cases driven by the thermal properties of the interface. Thermal exchanges with the gas and splat material properties play only a minor role in the cooling process.

- the computed flattening degrees are well below the theoretical previsions of Madejski's model [17]. The results of the simulations are reasonably fitted by a relation of Madejski's type (see Eq. (2)), but using a modified proportionality coefficient M equal to 0.925.

- the presence of unmelted material in the droplet is found to decrease even more the flattening degree, and it was seen that a simple model which assumes a decoupled behaviour for the melted and unmelted parts provides a good quantitative description of the phenomena.

More experimental information is clearly necessary to further improve and validate the model. Work is in progress to obtain relevant data.

In order to apply the model to lower viscosity materials an implementation of a mixed Lagrangean–Eulerian approach appears necessary. This development will complete the present computational model and allow its employment within the wide range of process parameters and material properties encountered in the plasma-spray manufacturing process.

ACKNOWLEDGMENTS

P. Fauchais, A. Vardelle, and M. Vardelle kindly allowed us access to unpublished data. We thank them, as well as J. H. Harding, for useful discussions. This work was supported by the BRITE/EURAM programme of the Commission of European Communities (Brite/Euram, BREU 0418 Fabercoat).

REFERENCES

1. J. H. Zaat, *Annu. Rev. Mater. Sci.* **13,** 9 (1983).
2. A. Vardelle, M. Vardelle, and P. Fauchais, *Rev. Int. Hautes Temp. Refract.* **23,** 69 (1986).
3. P. Fauchais, A. Grimaud, A. Vardelle, and M. Vardelle, *Ann. Phys. Paris Les Ulis* **14,** 261 (1989).

4. D. S. Rickerby, G. Eckold, K. T. Scott, and I. M. Buckley-Golder, *Thin Solid Films* **154,** 125 (1987).
5. R. McPherson, *Surf. Coating Technol.* **39–40,** 173 (1989).
6. J. Mishin, M. Vardelle, J. Lesinski, and P. Fauchais, *J. Phys. E* **20,** 620 (1987).
7. C. Moreau, P. Cielo, and M. Lamontagne, ''Flattening and Solidification of Thermal Sprayed Particles,'' in *Proceedings, International Thermal Spray Conference and Exposition, Orlando, Florida, 1992,* edited by ASM, p. 761.
8. S. Fantassi, M. Vardelle, P. Fauchais, and C. Moreau, ''Investigation of the Splat Formation versus Different Particulate Temperatures and Velocities Prior to Impact,'' in *Proceedings, International Thermal Spray Conference and Exposition, Orlando, Florida, 1992,* edited by ASM, p. 755.
9. A. M. Worthington, *A Study of Splashes,* (MacMillan Co., New York, 1963).
10. G. Trapaga, and J. Szekely, *Metall. Trans. B* **22,** 901 (1991).
11. G. Trapaga, E. F. Matthys, J. J. Valencia, and J. Szekely, *Metall. Trans. B* **23,** 701 (1992).
12. T. Yoshida, T. Okada, H. Hideki, and H. Kumaoka, *Plasma Sources Sci. Technol.* **1,** 195 (1992).
13. J. Fukai, Z. Zhao, D. Poulikakos, C. M. Megaridis, and O. Miyatake, *Phys. Fluids A* **5**(11), 2588 (1993).
14. Z. Kang, Z. Zhao, and D. Poulikakos, *Heat Transfer* **116,** 436 (1994).
15. O. Knotek, and R. Elsing, *Surf. Coating Technol.* **32,** 261 (1987).
16. S. Cirolini, J. H. Harding, and G. Jacucci, *Surf. Coating Technol.* **48,** 137 (1991).
17. J. Madejski, *J. Heat Mass Trans.* **19,** 1009 (1976).
18. S. Fantassi, M. Vardelle, A. Vardelle, and P. Fauchais, ''Influence of the Velocity of Plasma Sprayed Particles on the Splat Formation,'' in *Proceedings, NTSC' 93, Anaheim, CA,* ASM, Materials Park, OH, 1993.
19. J. M. Houben, ''Future Developments in Thermal Spraying,'' in *Proceedings, Second American Conference on Thermal Spray, Long Beach, CA,* p. 1–19 1984, (unpublished).
20. J. M. Houben, doctoral thesis, Technische Universiteit, Eindhoven, 1988 (unpublished).
21. G. Brant Foote, *J. Atmos. Sci.* **32,** 390 (1975).
22. J. Argyris, I. St. Doltsinis, H. Fischer, and H. Wüstenberg, *Comput. Methods Appl. Mech. Engng* **51,** 289 (1985).
23. I. St. Doltsinis, J. Luginsland, and S. Nölting, *Engng. Comput.* **4,** 266 (1987).
24. I. St. Doltsinis, *Engng. Comput.* **7,** 2 (1990).
25. I. St. Doltsinis, ''Coupled Field Problems—Solution Techniques for Sequential and Parallel Processing,'' in *Solving Large Scale Problems in Mechanics,* edited by M. Papadrakakis (Wiley, New York, 1993).
26. I. St. Doltsinis, and S. Nölting, *Comput. Systems Engng,* **2,** 427 (1992).
27. I. St. Doltsinis, M. Eggers S. Nölting, and G. Nötzel, 1st Work Report, ICA-Stuttgart, 1992 (unpublished).
28. M. Vardelle, A. Vardelle, P. Fauchais, and C. Moreau, *Meas. Sci. Technol.* **5,** 205 (1994).
29. Brite/Euram Project No. BREU-0418, Final Technical Report, European Union, Bruxelles, Belgium, 1995 (unpublished).
30. J. H. Harding, private communication, AEA Technology, Harwell Laboratory, UK, 1993.
31. J. L. Fink, M. G. Chasanov, and L. Leibowitz, ANL-CEN-RSD-80-4, Argonne National Laboratory Report, 1981 (unpublished).
32. J. Fukai, Y. Shiiba, T. Yamamoto, O. Miyatake, D. Poulikakos, C. M. Megaridis, and Z. Zhao, *Phys. Fluids* **7**(2), 236 (1995).
33. R. Westhoff, G. Trapaga, and J. Szekely, *Metall. Trans. B* **23,** 683 (1992).
34. H. Wüstemberg, ICA Report No. 21, Stuttgart; ICA Report No. 22, Stuttgart, 1986 (unpublished).
35. C. San Marchi, H. Liu, E. J. Lavernia, R. H. Rangel, A. Sickinger, and E. Muehlberger, *J. Mater. Sci.* **28,** 3313 (1993).